Journal of Alloys and Compounds 1056 (2026) 186542

Contents lists available at ScienceDirect

Journal of Alloys and Compounds

journal homepage: www.elsevier.com/locate/jalcom

Mechanochemistry-assisted construction of strong metal−support interactions in core-shell metal@BN toward enhanced hydrogen generation

Miao Guo, Chongyang Yuan, Xuebin Yu *

Department of Materials Science, Fudan University, Shanghai 200433, China

ARTICLE INFO

Keywords:
Heterogeneous catalyst
Strong metal−support interactions
Hexagonal boron nitride
Core-shell structure
Platinum

ABSTRACT

Among various heterogeneous catalysts, the strong metal–support interaction (SMSI)-based catalysts have demonstrated remarkable activity in many fields. However, most of the classical SMSI catalysts reported so far are based on oxide supports and are formed under harsh reduction conditions and high temperatures. Herein, a metal/BN core–shell structure based on SMSI is reported by the reduction reaction of metal ions on hBN modified by a simple ball-milling process. This effective method can be further generalized to load various noble or non-noble metal nanoparticles (Co, Ni, Fe, Cu, and Pt) on modified hBN. Both experimental results and theoretical calculations show that hBN with good crystallization after ball milling tends to become amorphous, and the adsorption between the amorphous BN and metal nanoparticles is significantly enhanced. Due to the formation of the SMSI shell, the Pt on modified hBN sample showed enhanced catalytic performance for the hydrogen production via hydrolysis of ammonia borane. Compared with Pt on pristine hBN, the catalytic turnover frequency of Pt on modified hBN catalyst is increased by 4 times to 366.9 min^{-1} and shows twice the stable catalytic duration, both of which are predominant among most Pt-based catalysts reported so far.

1. Introduction

Nowadays with the development of both traditional chemical manufacturing and the new energy industry, heterogeneous catalysts always play an essential role and are widely implemented in these fields due to their advantages such as easy separation and reusability [1–3]. Among various kinds of heterogeneous catalysts, the nanocatalysts composed of metal nanoparticles (NPs) and supports with strong metal−support interactions always exhibit high performance and gain considerable attention from researchers in many catalysis applications including thermocatalysis, electrocatalysis and photocatalysis [4–6]. The traditional SMSI-based catalysts display an encapsulation and coverage structure with a metal NP core and a thin suboxide shell which is produced by the support under high temperature or some reducing conditions. The production of suboxides and reducing electrons can lead to a decreased surface energy of metal NPs, thus the metal NPs are easily encapsulated and covered. On account of the protection of this SMSI shell, the SMSI-involved catalysts have the advantage of favorable stability. Moreover, the geometric and electronic structures of the encapsulated metal NPs can be modulated by the SMSI overlayer and reducible supports so that the activation of reactants and catalytic performance are boosted. Therefore, the SMSI effect adds to the versatility and robustness of nanocatalysts. Nevertheless, at present, most reported classical SMSI catalysts are based on oxide supports, and it is commonly believed that SMSI between metal NPs and inert oxides like MgO barely occurs, not to mention the inert nonoxide supports such as graphene and hexagonal boron nitride (hBN) [7].

hBN is a typical two-dimensional material with some unique chemical and physical properties. hBN has excellent thermal stability, good electrical insulation, high temperature resistance, corrosion resistance and good mechanical properties [8–10]. However, its chemical inertness restricts the functionalization of hBN particularly in applications such as strong metal support interaction SMSI in nanocatalysts. So far, only a few reported of hBN-based SMSI catalysts are achieved from high-temperature reaction conditions (specifically, >700 °C) [11,12]. For example, Dong et al. found that a boron oxide (BO_x) shell can be derived from hBN support. And because of the weak oxidizability of CO_2 and H_2O, the formation of this BO_x shell is induced in the dry reforming of methane process at 750 °C; another example is Pd/h-BN-SMSI fabricated through an 850 °C thermal treatment. These explorations demonstrate the improved catalytic activity and robust stability of hBN-based nanocatalysts due to the function of SMSI. Even though these

* Corresponding author.
E-mail address: yuxuebin@fudan.edu.cn (X. Yu).

https://doi.org/10.1016/j.jallcom.2026.186542
Received 16 December 2025; Received in revised form 19 January 2026; Accepted 30 January 2026
Available online 30 January 2026

improvements have been realized, effective SMSI construction with hBN under ambient conditions for high-performing catalysts is still lacking and remains essential, and understanding the driving forces of SMSI formation is also needed in greater detail.

Ball milling, as a typical mechanochemistry method in large-scale synthesis, has gradually been applied in synthesizing various classes of novel nanomaterials through mechanical force-derived physical and chemical reactions [13–15]. Recently, ball milling has been used to manufacture numerous nanocatalyst materials, including metal phosphides [16], high entropy oxides [17], metal-organic frameworks (MOFs) [18,19], hydrogen-bonded organic frameworks (HOFs) [20], supported noble metal catalysts [21–23] as well as single-atom catalysts [24,25]. In addition, lots of material modification methods, for instance, defect engineering [26,27], heterogeneous structure construction [28,29] and decrystallization engineering [13,30,31] have been found to be carried out by ball milling owing to its high-power mechanical force. Therefore, it is a very feasible approach to use ball-milling to modify the support material like hBN. On the basis of the strong structural destruction due to the high-power mechanochemical force of ball milling, modified hBN must exhibit some unusual and interesting properties.

Herein, a simple mechanochemistry-assisted approach was developed for a novel SMSI construction under mild conditions. After ball milling, it is discovered that a metal/BN core-shell structure based on SMSI can be formed through the reduction of metal ions on the modified hBN (hereafter called 10BN). This unique phenomenon was first found for hBN-supported catalysts and put forward as a new type of strong metal−support interactions with milder conditions. Besides, this facile and efficient method could be further extended to support various noble or non-noble metal NPs (Co, Ni, Fe, Cu and Pt) on the 10BN. Both experimental results and theory calculations indicate that the chemically stable hBN tends to be an amorphous state after ball milling so that an increased adsorption energy between 10BN and metal NPs is realized. In this way, the SMSI-based core-shell structure of metal@10BN is easily to create. And owing to the foundation of SMSI shell, the metal@10BN samples display an enhanced catalytic activity and improved stability for catalytic hydrogen generation from ammonia borane (AB) hydrolysis.

2. Experiment

2.1. Chemical and materials

$CoCl_2{\cdot}6H_2O$ (99 %, Aladdin), $NiCl_2{\cdot}6H_2O$ (99 %, Aladdin), $FeCl_3{\cdot}6H_2O$ (99 %, Aladdin), $CuCl_2{\cdot}6H_2O$ (99 %, Aladdin), $H_4PtCl_6{\cdot}6H_2O$ (Aladdin), methanol, hBN (99.9 %, Aladdin), $NaBH_4$ (99 %, Aladdin), ammonia borane (NH_3BH_3, 97 %, Rhawn).

2.2. Preparation of amorphous boron nitride

*x*BN is obtained from commercially purchased hexagonal boron nitride after ball milling at 600 rpm for *x* h under 1 atm of argon using a planetary ball mill (Fritsch, P7). The ball-to-sample ratio was approximately 40:1. The milling process was conducted by alternating 30 min of milling with 15 min pause to minimize the temperature increase.

2.3. Preparation of M@10BN (M = Pt, Fe, Co, Ni, Cu)

First, 16 mg $H_2PtCl_6{\cdot}6\ H_2O$, 90 mg 10BN and 50 mL deionized water were added into a 100 mL beaker (with a theoretical Pt loading of 5 wt %) and stirred with ultrasound for 30 min to form a uniform dispersion solution. Next, 20 mg $NaBH_4$ was dissolved in 2 mL deionized water to prepare a uniform solution. Then, the $NaBH_4$ aqueous solution was quickly added to the BN dispersion and stirred for 12 h. The dispersion changed from greyish to black. Afterward, the black dispersion was centrifuged and washed with ethanol three times. Finally, the separated black powder was dried at 60 °C under vacuum for 12 h to remove excess ethanol and the sample named Pt@10BN was obtained. For the preparation of *M*@10BN (*M* = Fe, Co, Ni, Cu), $H_2PtCl_6{\cdot}6\ H_2O$ was simply replaced with $Co(NO_3)_2{\cdot}6\ H_2O$, $Ni(NO_3)_2{\cdot}6\ H_2O$, $Cu(NO_3)_2{\cdot}3\ H_2O$, or $Fe(NO_3)_3{\cdot}9\ H_2O$. The metal content in each *M*@10BN sample was determined by ICP-OES (Table S1).

2.4. Characterizations of catalysts

Powder X-ray diffraction pattern (PXRD) was carried out with a Rigaku D/max 2000 diffractometer with monochromatized Cu Kα radiation (λ = 1.5418 Å) at a scan rate of 10° min^{-1}. Scanning electron microscope (SEM) was performed on a Hitachi S-4800 electron microscope with acceleration voltage of 1 kV. Transmission electron microscope (TEM) was operated by a Hitachi-7700 working at 100 kV. HRTEM and HAADF-STEM were carried out by a JEOL JEM-2100F field emission electron microscope working at 200 kV. Atomic resolution HAADF-STEM images were obtained by using a Titan 80–300 scanning/transmission electron microscope operated at 200 kV, equipped with a probe spherical aberration corrector. Inductively coupled plasma optical emission spectrometry (ICP-OES) was using a Thermo Fisher iCAP PRO. X-ray photoelectron spectroscopy (XPS) was performed on a Thermo Scientific K-Alpha using a 200 W monochromated Al Kα radiation.

2.5. Catalytic activity evaluation

For the hydrogen generation test of AB hydrolysis, firstly, a certain amount of catalyst (typically 10 mg) was added to a 50 mL two−necked flask containing 5 mL water, followed by an ultrasonication treatment for 20 min. Then, the flask reactor was kept at a certain temperature (typically 298 K) by a water bath. Finally, the reaction started when 1 mmol AB which was dissolved in 5 mL NaOH aqueous solution (1 mol L^{-1}) was injected into the flask by using a syringe under stirring conditions. The volume of generated H_2 was recorded by a flowmeter (Ritter MGC−1 V3.4 PMMA) connected with a computer. The hydrogen was exhausted to the outside to ensure safety. The test was finished with no more gas was generated. For the durability experiments, the catalyst was recovered and reused for the next cycle under the same conditions. The reaction was completed when there was no more gas generated. The catalytic activity of samples was evaluated by TOF value:

$$\mathrm{TOF} = \frac{n_{H_2}}{n_{\mathrm{metal}} * t} \tag{2}$$

in which n_{H_2} is the mole number of generated H_2, n_{metal} is the mole number of metal element in the catalysts, *t* is the reaction time in unit of minutes. For the stability experiments, a long-term catalytic activity was tested in 10 mL of aqueous AB solution (10 M) at 298 K over 5 mg of catalyst. The TON value was calculated based on the number of total noble metal atoms in catalysts and the number of generated H2 from AB hydrolysis. The calculation equation used was as follows:

$$\mathrm{TON} = \frac{n_{H_2}}{n_{\mathrm{metal}}} \tag{3}$$

2.6. Calculation

Ab initio Molecular Dynamics (AIMD): In this study, the AIMD method was used to construct the amorphous boron nitride (BN) structure. Only the gamma point of the Brillouin zone was considered to reduce computational demands. Standard ensemble conditions (NVT) were achieved using the Nosé-Hoover thermostat, with the temperature set to 5000 K and a time step of 1 fs. For the initial structure, a 5 ps MD simulation was performed to equilibrate the system, and then the temperature was reduced to 298 K and maintained for 5 ps. This resulted in a single layer of amorphous BN. For the AIMD process of the structure, the energy and force convergence criteria were set to 10 −4 eV and 0.05 eV/Å, respectively, and the plane-wave cutoff energy was set to

400 eV. The Brillouin zone for the entire periodic structure was sampled based on the gamma (Γ) point grid size. To describe the van der Waals (vdW) weak interactions between the intermediate and the substrate, the Grimme DFT-D3 density functional empirical dispersion correction method was used. A vacuum layer of at least 20 Å along the z-direction was applied to avoid interlayer interference.

All Density Functional Theory (DFT) calculations in this chapter used the Vienna Ab initio Simulation Package (VASP) software [32–37]. The PBE functional was used to simulate exchange-correlation interactions, and the PAW method was applied to describe ion-electron interactions. The empirical DFT-D3 method was used to include vdW interactions. For all periodic structures, the Monkhorst-Pack grid-based k-point mesh for the Brillouin zone was set to 3 × 3 × 1, with a cutoff energy of 450 eV. The convergence criteria for forces and energies were 0.01 eV $Å^{-1}$ and 10^{-5} eV, respectively. A vacuum layer of at least 20 Å along the z-direction was applied to avoid interlayer interference. The binding energy ($\Delta E_{binding}$) was calculated using the formula $\Delta E_{binding} = E_{substrate} + E_{adsorbate} - E_{total}$, where $E_{substrate}$ is the energy of the substrate, $E_{adsorbate}$ is the energy of the adsorbate, and E_{total} is the total energy of the adsorption system.

3. Results and discussion

3.1. Mechanochemistry-assisted approach and characterization of ball milled BN

As stated above, hBN has attracted tremendous attention owing to the exceptional properties and immense application potential. Therefore, hBN is selected as a promising support in SMSI-based catalysts and will lead to favorable catalytic performance. The *M*@10BN with a core-shell structure was constructed by a ball-milling assisted approach as shown in Fig. 1. A key step is the preparation of amorphous BN through ball-milling treatment. After ball milling, a typical metal particle reduction process is carried out. Thanks to the strong reducing properties of $NaBH_4$, the different metal particles can be reduced from metal ionic state. Finally, the *M*@10BN will be formed during the reduction process.

As for the synthesized milled BN sample, the different ball-milling times were adopted to obtain the milled BN with various degrees of crystallinity. As shown in Fig. 2a and Fig. S1, it is evident that the crystallinity of these BN samples decreases with increasing ball-milling time. Moreover, the milled BN turns amorphous when the ball milling process exceeds 10 h. Similarly, the specific surface area changes with different ball-milling time (Fig. S2). The 3BN, with ball-milling time of three hours, exhibits the highest specific surface area of 364.9 $m^2\ g^{-1}$. However, when the ball-milling time is increased to 6, 10 and 12 h, the specific surface area decreases to 209.3, 175.8 and 79.2 $m^2\ g^{-1}$, respectively. Based on the crystallinity and specific surface area of different milled BN, as shown in Fig. 2d, 10BN, with an amorphous phase and a higher specific surface area of 175.8 $m^2\ g^{-1}$ than hBN precursor of 28.4 $m^2\ g^{-1}$, was chosen as the modified support. Furthermore, from the SEM images in Fig. 2b-c, hBN precursor exhibits a regular two-dimensional sheet structure. In contract, the 10BN shows a random morphology because of the destruction of strong mechanical force from high energy ball milling. Additionally, HRTEM images identify the details of hBN precursor and 10BN at the atomic level. Fig. 2e confirms the amorphous phase of 10BN whereas Fig. 2f shows the high crystallinity of hBN precursor with a clear lattice spacing of 0.221 nm, corresponding to the (100) plane. The inset graph represents fast fourier transform (FFT) image, further confirming the high crystallinity of hBN precursor and the amorphization of 10BN.

3.2. Characterization of various core-shell metal@10BN nanocatalysts

After 10BN was selected as the carrier material, different metal nanoparticles were loaded on 10BN according to the method (Fig. 1). Fig. S3 shows the obtained XRD patterns of different *M*@10BN (*M* = Pt, Fe, Co, Ni, Cu). The corresponding metal XRD peaks are observed in the XRD of Pt@hBN, Pt@10BN, and Cu@10BN samples, as shown in Fig. S3a, indicating the successful loading of Pt and Cu nanoparticles. However, there is no obvious diffraction peak in XRD of Fe@10BN, Co@10BN and Ni@10BN samples, as shown in Fig. S3b, indicating that Fe, Co and Ni nanoparticles are present as amorphous structures, which is caused by the different reductivities of different metal elements during the reduction process of sodium borohydride [38]. Due to the weak reductivity of Pt and Cu, they are easier to be reduced to form a better crystal structure. In contrast, Fe, Co and Ni can only be reduced to form an amorphous structure because of their strong reducibility. This is further confirmed by subsequent high-resolution TEM images.

In order to further explore the composition and structure of *M*@10BN samples, the TEM, XPS and EDX of different samples were conducted, and the results are shown in Fig. 3 and S4. The microstructure of Pt@hBN, Pt@10BN and Cu@10BN samples exhibit good crystallinity of metal nanoparticles. Noteworthily, not only are Pt, Cu

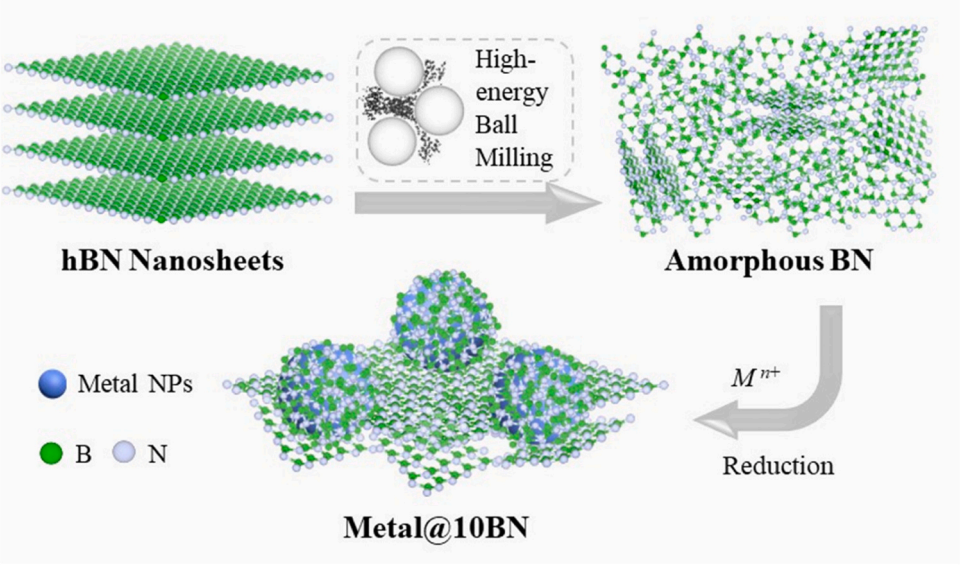

Fig. 1. Schematic illustration of the construction of core-shell boron nitride / metal nanoparticles by the mechanochemistry-assisted SMSI method.

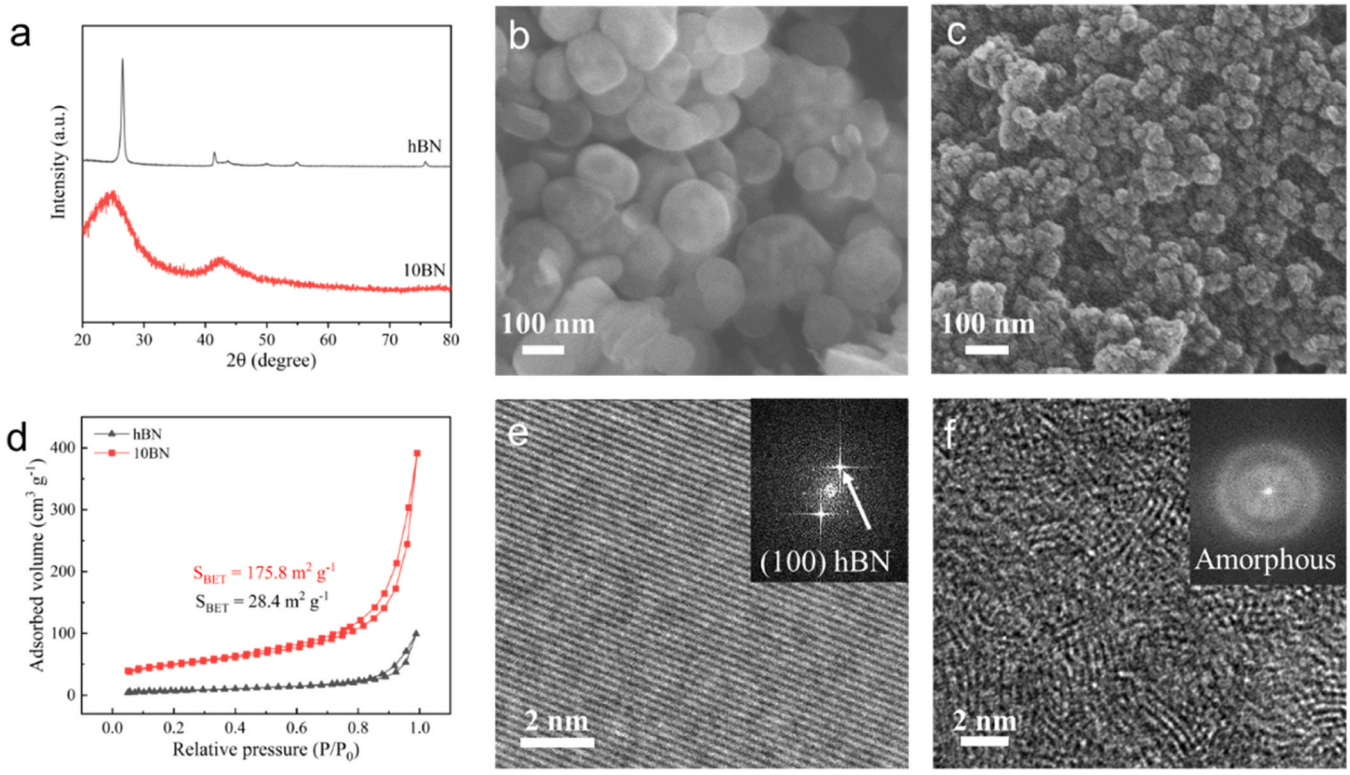

Fig. 2. Characterization of hBN after ball milling. (a) XRD patterns and (d) N2 adsorption-desorption isotherms of hBN and 10BN. SEM and HRTEM images of (b, e) hBN and (c, f) 10BN, inset graph is FFT image.

nanoparticles successfully loaded on boron nitride, but also a coating structure with metal nanoparticles as the core and BN as the shell was observed in Pt@10BN and Cu@10BN samples. It can be seen that the thickness of the BN shell is about 2.5 nm, and it is evenly coated on the surface of the metal nanoparticles, similar to putting on an armor to the metal particles. The Pt NPs with ~5 nm are covered by a BN layer with a thickness of ~2.5 nm in the Pt@10BN sample. The corresponding elemental mapping of Pt@10BN in Fig. 3g also proves the formation and loading of Pt species on the 10BN support. Pt 4 f XPS spectrum further reveals the formation of the Pt NPs. The binding energies can be deconvoluted into six peaks in Fig. 3d: the peaks of 71.2 eV and 74.5 eV, 72.2 eV and 75.6 eV, 73.0 eV and 76.7 eV, are attributed to Pt^0, Pt^{2+}, Pt^{4+}species, respectively.

Moreover, the same coating structure also exists in the samples Fe@10BN, Co@10BN and Ni@10BN. Metal particles with an average size of around 30 nm are coated by an amorphous boron nitride shell with a thickness of about 2.5 nm. However, Pt nanoparticles are uniformly loaded on hBN support in the Pt@hBN sample, without similar boron nitride shell, indicating that this is a unique SMSI between metal particles and amorphous BN. In addition, the metal particles in Fe@10BN, Co@10BN, and Ni@10BN samples do not show regular lattice fringes under high-resolution TEM, indicating that Fe, Co, and Ni nanoparticles are amorphous, which is consistent with XRD results in Fig. S3. The XPS results of different samples also show the successful preparation of metal particles, which are mainly composed of metallic elements and a small portion of metal oxidation states, consistent with the expected experimental results. EDX elemental analysis also demonstrates that different metal nanoparticles were successfully combined with boron nitride, and the element distribution is uniform.

3.3. Catalysis performance for AB hydrolysis

Composite supports induced from the nanoscale architecture design could always bring unique and tunable properties to the nanomaterials with enhanced catalytic performance. To evaluate the activity and stability of the core-shell structure demonstrated herein in supporting metal nanoparticle catalysts, the catalytic performances of *M*@10BN (*M* = Pt, Fe, Co, Ni, Cu) samples for hydrolytic hydrogen evolution from 1 mmol AB at room temperature are shown in Fig. 4a-b. Pt@10BN shows the highest catalytic activity. It only takes about 5 min to catalyze the complete dehydrogenation of 1 mmol of AB, and the TOF value is as high as 366.9 min^{-1}, which is higher than most Pt-based catalysts reported so far (Table S2 and Fig. 4**i**) [39]. The catalytic activity of different metals is as follows: Pt@10BN > Co@10BN > Ni@10BN > Cu@10BN > Fe@10BN. Fe@10BN has almost no activity for AB hydrolysis. Fig. 4c-d shows the comparison of catalytic performance between Pt nanoparticles loaded on well-crystallized hBN (Pt@hBN) and Pt nanoparticles loaded on amorphous boron nitride (Pt@10BN). Under the same conditions, the complete catalytic reaction time of Pt@10BN is around one quarter of that of Pt@hBN sample, indicating that the catalytic reaction rate of Pt@10BN is over four times that of Pt@hBN. The TOF value of Pt@hBN is only 81.5 min^{-1}, while Pt@10BN shows a superior TOF of 366.9 min^{-1}. Meanwhile, it is obvious that there is no catalytic activity of the different BN support as shown in Fig. S6. Thus, amorphous boron nitride increases the catalytic activity of Pt particles by more than 4 times, which proves that the coating structure formed between metal particles and amorphous boron nitride had a positive effect on the catalytic activity. On the one hand, the amorphous BN support inhibits the growth of metal nanoparticles and regulates the size of metal particles as shown in Fig. S5. The intense aggregation effect causes the Pt particle size to reach about 12.3 nm in Pt@hBN, while the Pt nanoparticles are more evenly distributed with a particle size of about 8.8 nm in Pt@10BN. On the other hand, amorphous BN can significantly influence the electronic structure of Pt as the XPS results shown in Fig. 3d and Fig. S4h. Compared to Pt@hBN, the Pt peaks of Pt@10BN shift to higher energy and exhibit more oxidation states, indicating that amorphous BN causes Pt lose more electrons, which facilitates the adsorption of intermediates in the catalytic reaction and promotes the

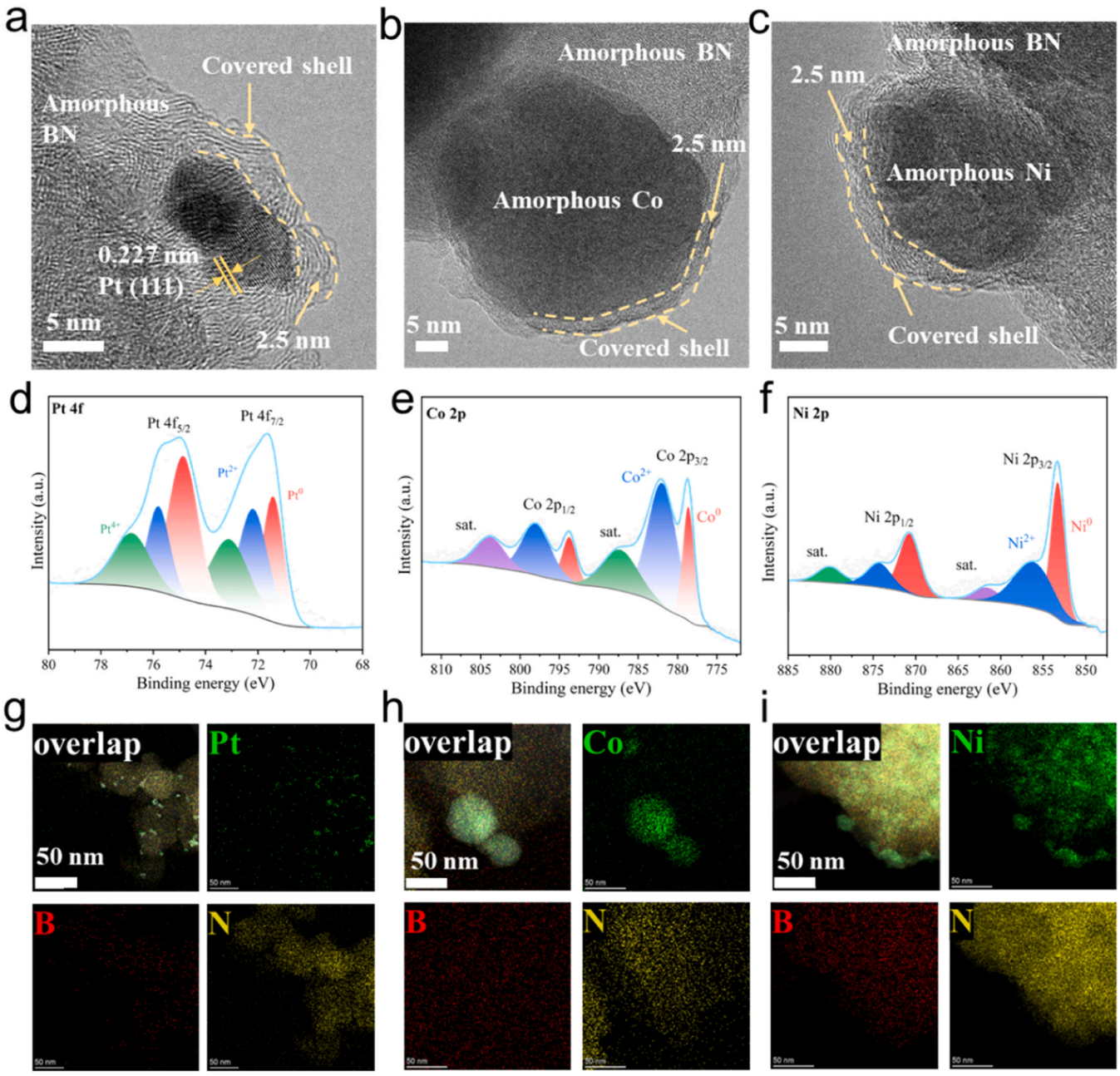

Fig. 3. (a-c) HRTEM images, (d-f) fine XPS spectra of Pt4f, Co2p and Ni2p orbits, and (g-i) EDX element analysis of samples Pt@10BN, Co@10BN, and Ni@10BN.

dissociation of reaction products. Besides, the high specific surface area of amorphous boron nitride promotes the contact between the reaction substrate and the catalytic active center. Therefore, the catalytic performance of Pt is greatly improved. Moreover, the SMSI effect between amorphous boron nitride and Pt particles can also improve the stability of Pt catalyst. As shown in Fig. 4h, under long-term catalytic hydrolysis of AB, the activity of Pt@hBN gradually disappeared after about 5 h, while the deactivation of Pt@10BN occurred after nearly 10 h. The total turnover number (TON) of Pt@10BN is 139277 mol_{H2} mol_{Pt}^{-1}, much higher than that of Pt@hBN (26213 mol_{H2} mol_{Pt}^{-1}). Fig. S7 summarizes the protective effect of the amorphous boron nitride coating structure. There are two main protective effects, one is to avoid agglomeration deactivation of nanoparticles, the other is to prevent harmful adsorption of boron species. These two aspects of synergistic protection improve the stability of metal particles.

Fig. 4e-f shows the catalytic hydrogen evolution curves of AB hydrolysis for Pt@10BN and Pt@hBN at different temperatures. Through kinetic fitting of the catalytic performance at different temperatures, it is found that Pt@10BN has a lower apparent activation energy for AB hydrolytic hydrogen production, which is 31.8 kJ mol^{-1}, much smaller than that of Pt@hBN (61.9 kJ mol^{-1}), as shown in Fig. 4g. Therefore, kinetic investigation reveals that the Pt@10BN catalyst has a more favorable catalytic reaction kinetic process than the Pt@hBN catalyst.

3.4. Formation mechanism of SMSI induced by amorphous boron nitride

Due to the formation of a unique core-shell structure between amorphous boron nitride and metal nanoparticles, which acts as an "armor" for the metal particles, it not only prevents particle aggregation and growth to achieve a uniform dispersion of metal nanoparticles, but also prevents the adsorption of boron species on the surface of the metal nanoparticles, which may result in the deactivation of the catalyst. Accordingly, the catalytic activity and stability of the metal nanoparticles are greatly enhanced. As shown in Fig. 5a and Fig. S8, the

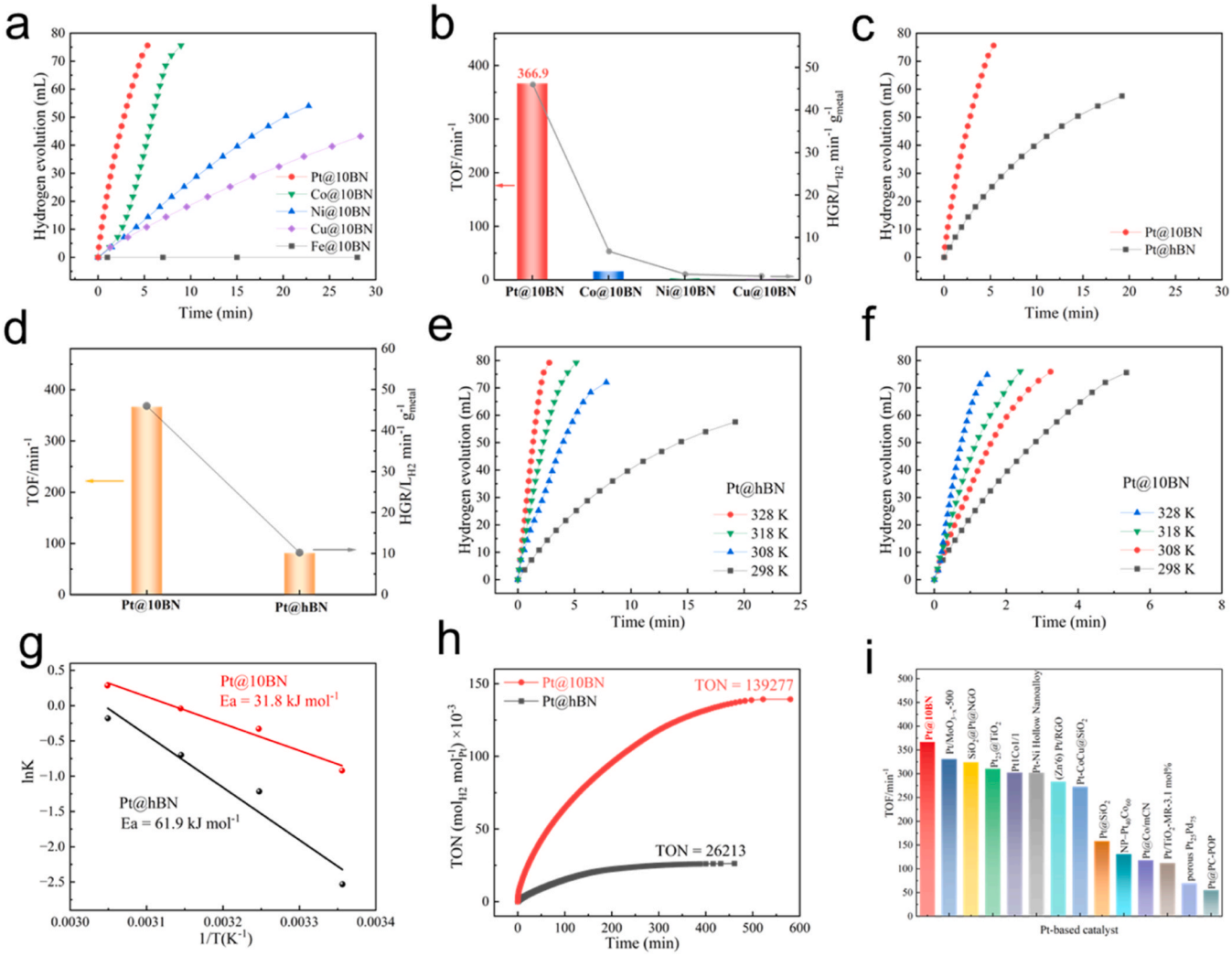

Fig. 4. (a) Curves of H_2 generation produced of 1 mmol AB at 298 K catalyzed by *M*@10BN with different metal and (b) corresponding TOF and HGR. (c) Curves of H_2 generation produced of 1 mmol AB at 298 K catalyzed by Pt@10BN and Pt@hBN with (d) corresponding TOF and HGR. Hydrogen evolution for AB hydrolysis at different temperatures in the range of 298 −313 K of (e) Pt@hBN and (f) Pt@10BN; (g) the corresponding linear fitting of the Arrhenius equation between ln k and 1/T. (h) Hydrogen release performance of Pt@10BN and Pt@hBN under long-term stability at 298 K. (i) Compare of Pt-based catalysts reported so far.

formation of this core-shell structure between the amorphous boron nitride support and the metal is different from the interaction between traditional metal-oxide supports or hexagonal boron nitride supports, as it does not require high temperatures or highly reducing gases. Instead, it can be formed under room-temperature and standard reduction conditions.

To gain insight into the SMSI mechanism induced by amorphous boron nitride, the interaction strengths between Pt nanoparticles and well-crystallized or amorphous boron nitride were systematically calculated (Fig. 5). The adsorption energy between amorphous boron nitride and Pt nanoparticles is 2.55 eV, much higher than the adsorption energy between crystalline boron nitride and Pt nanoparticles (0.75 eV). This indicates that amorphous boron nitride more readily adsorbs onto the surface of Pt nanoparticles, ultimately forming the core-shell structure, while controlling the size of Pt nanoparticles to prevent further growth. In contrast, the adsorption interaction between crystalline boron nitride and Pt nanoparticles is weaker, making it unable to form a core-shell structure and having a limited effect on inhibiting the aggregation and growth of Pt nanoparticles during catalysis.

4. Conclusion

In summary, a new type of metal–support interaction induced by amorphous boron nitride is demonstrated. This interaction simultaneously enhances both the catalytic activity and stability of Pt nanoparticles. By employing the strong mechanical force generated during high-energy ball milling, well-crystallized hexagonal boron nitride is transformed into an amorphous phase. Subsequently, various metal nanoparticles are successfully deposited onto amorphous boron nitride via a chemical reduction route, leading to the formation of a unique core–shell structure consisting of a metal core encapsulated by an amorphous boron nitride shell. When applied to hydrogen generation from ammonia borane hydrolysis, the resulting catalyst exhibits excellent catalytic performance. In comparison with Pt@hBN, Pt@10BN delivers approximately fourfold and fivefold enhancements in catalytic activity and stability, respectively. These improvements are primarily attributed to the strong interaction between amorphous boron nitride and Pt nanoparticles. On the one hand, the amorphous boron nitride coating regulates the size of Pt nanoparticles and increases the effective contact area for catalytic reactions. On the other hand, it suppresses particle agglomeration and inhibits the detrimental adsorption of boron species. As a result, the overall catalytic properties of Pt@10BN are

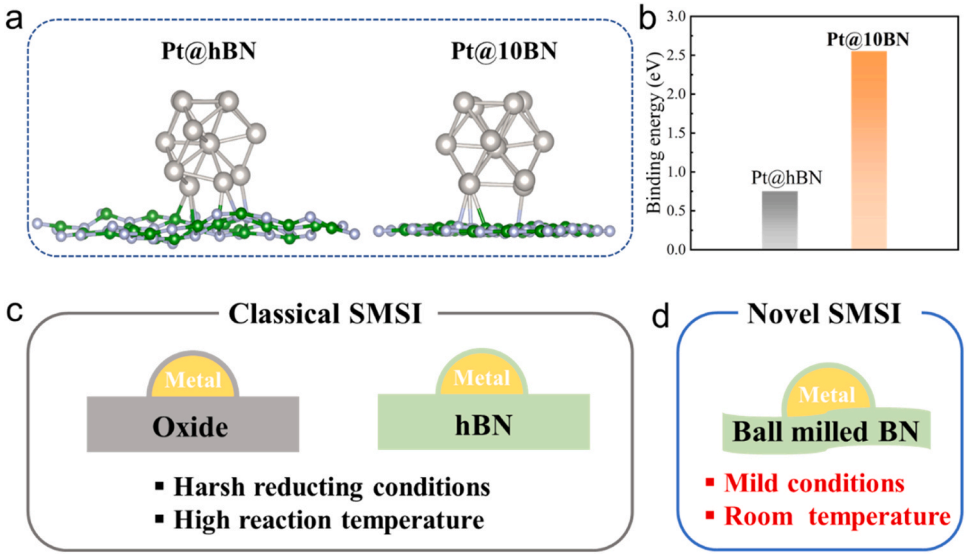

Fig. 5. (a) The scheme and (b) corresponding values of adsorption energy between Pt nanoparticles and hBN/10BN; (c) classical SMSI in metal/oxide and metal/hBN catalysts; (d) novel SMSI in metal/ball milled BN catalysts.

significantly improved. Furthermore, theoretical simulations reveal that the stronger adsorption between amorphous boron nitride and Pt nanoparticles facilitates the formation of the coating structure, providing microscopic insight into the origin of this novel SMSI.

CRediT authorship contribution statement

Xuebin Yu: Writing – review & editing, Investigation, Funding acquisition. **Chongyang Yuan:** Writing – original draft, Formal analysis, Data curation, Conceptualization. **Miao Guo:** Writing – original draft, Formal analysis, Data curation.

Declaration of Competing Interest

The authors declare that they have no known competing financial interests or personal relationships that could have appeared to influence the work reported in this paper.

Acknowledgements

This work was supported by National Sciences Foundation of China (51971065) and the Innovation Program of Shanghai Municipal Education Commission (2019–01–07–00–07-E00028).

Appendix A. Supporting information

Supplementary data associated with this article can be found in the online version at doi:10.1016/j.jallcom.2026.186542.

References

[1] G. Wu, Y. Liu, J. Wang, Oxidative-atmosphere-induced strong metal-support interaction and its catalytic application, Acc. Chem. Res. 56 (2023) 911–923.
[2] Y. Qi, B. Zhang, G. Zhang, Z. Zheng, T. Xie, S. Chen, G. Ma, C. Li, K. Domen, F. Zhang, Efficient overall water splitting of a suspended photocatalyst boosted by metal-support interaction, Joule 8 (2024) 193–203.
[3] D. Xu, S.-N. Zhang, J.-S. Chen, X.-H. Li, Design of the synergistic rectifying interfaces in Mott–Schottky catalysts, Chem. Rev. 123 (2023) 1–30.
[4] M. Xu, M. Peng, H. Tang, W. Zhou, B. Qiao, D. Ma, Renaissance of strong metal–support interactions, J. Am. Chem. Soc. 146 (2024) 2290–2307.
[5] S.K. Kaiser, E. Fako, I. Surin, F. Krumeich, V.A. Kondratenko, E.V. Kondratenko, A. H. Clark, N. Lopez, J. Perez-Ramirez, Performance descriptors of nanostructured metal catalysts for acetylene hydrochlorination, Nat. Nanotechnol. 17 (2022) 606–612.
[6] H. Wang, L. Wang, D. Lin, X. Feng, Y. Niu, B. Zhang, F.-S. Xiao, Strong metal–support interactions on gold nanoparticle catalysts achieved through Le Chatelier's principle, Nat. Catal. 4 (2021) 418–424.
[7] H. Tan, B. Tang, Y. Lu, Q. Ji, L. Lv, H. Duan, N. Li, Y. Wang, S. Feng, Z. Li, C. Wang, F. Hu, Z. Sun, W. Yan, Engineering a local acid-like environment in alkaline medium for efficient hydrogen evolution reaction, Nat. Commun. 13 (2022) 2024.
[8] S. Ozden, N.S. Dutta, K. Randazzo, T. Tsafack, C.B. Arnold, R.D. Priestley, Interfacial engineering to Tailor the properties of multifunctional ultralight weight hBN-polymer composite aerogels, ACS Appl. Mater. Interfaces 13 (2021) 13620–13628.
[9] X. Fan, S.W. Kim, J. Tang, X. Huang, Z. Lin, L. Zhu, L. Li, J.H. Cho, C. Zeng, Spontaneous folding growth of graphene on h-BN, Nano Lett. 21 (2021) 2033–2039.
[10] Y. Wu, Y. Xue, S. Qin, D. Liu, X. Wang, X. Hu, J. Li, X. Wang, Y. Bando, D. Golberg, Y. Chen, Y. Gogotsi, W. Lei, BN nanosheet/polymer films with highly anisotropic thermal conductivity for thermal management applications, ACS Appl. Mater. Interfaces 9 (2017) 43163–43170.
[11] J. Dong, Q. Fu, H. Li, J. Xiao, B. Yang, B. Zhang, Y. Bai, T. Song, R. Zhang, L. Gao, J. Cai, H. Zhang, Z. Liu, X. Bao, Reaction-induced strong metal–support interactions between metals and inert boron nitride nanosheets, J. Am. Chem. Soc. 142 (2020) 17167–17174.
[12] H. Chen, S.Z. Yang, Z. Yang, W. Lin, H. Xu, Q. Wan, X. Suo, T. Wang, D.E. Jiang, J. Fu, S. Dai, Sinter-resistant nanoparticle catalysts achieved by 2D boron nitride-based strong metal-support interactions: a new twist on an old story, ACS Cent. Sci. 6 (2020) 1617–1627.
[13] J. Huot, D.B. Ravnsbæk, J. Zhang, F. Cuevas, M. Latroche, T.R. Jensen, Mechanochemical synthesis of hydrogen storage materials, Prog. Mater. Sci. 58 (2013) 30–75.
[14] T. Friscic, C. Mottillo, H.M. Titi, Mechanochemistry for Synthesis, Angew. Chem. Int. Ed. 59 (2020) 1018–1029.
[15] V. Martinez, T. Stolar, B. Karadeniz, I. Brekalo, K. Uzarevic, Advancing mechanochemical synthesis by combining milling with different energy sources, Nat. Rev. Chem. 7 (2023) 51–65.
[16] S. Ji, C. Song, J. Li, K.S. Hui, W. Deng, S. Wang, H. Li, D.A. Dinh, X. Fan, S. Wu, J. Zhang, F. Chen, Z. Shao, K.N. Hui, Metal phosphides embedded with in situ-formed metal phosphate impurities as buffer materials for high-performance potassium-ion batteries, Adv. Energy Mater. 11 (2021) 2101413.
[17] S. Hou, X. Ma, Y. Shu, J. Bao, Q. Zhang, M. Chen, P. Zhang, S. Dai, Self-regeneration of supported transition metals by a high entropy-driven principle, Nat. Commun. 12 (2021) 5917.
[18] J. Fan, T. Wang, H. Chen, Z. Wang, B.P. Thapaliya, T. Kobayashi, Y. Yuan, I. Popovs, Z. Yang, S. Dai, Mechanochemistry-driven construction of Aza-fused π-conjugated networks toward enhanced energy storage, Adv. Funct. Mater. 32 (2022) 2202669.
[19] W. Xu, H. Chen, K. Jie, Z. Yang, T. Li, S. Dai, Entropy-driven mechanochemical synthesis of polymetallic zeolitic imidazolate frameworks for CO2 fixation, Angew. Chem. Int. Ed. 58 (2019) 5018–5022.
[20] W.K. Qin, D.H. Si, Q. Yin, X.Y. Gao, Q.Q. Huang, Y.N. Feng, L. Xie, S. Zhang, X. S. Huang, T.F. Liu, R. Cao, Reticular synthesis of hydrogen-bonded organic frameworks and their derivatives via mechanochemistry, Angew. Chem. Int. Ed. Engl. 61 (2022) e202202089.
[21] R. Li, Z. Liu, Q.T. Trinh, Z. Miao, S. Chen, K. Qian, R.J. Wong, S. Xi, Y. Yan, A. Borgna, S. Liang, T. Wei, Y. Dai, P. Wang, Y. Tang, X. Yan, T.S. Choksi, W. Liu, Strong metal-support interaction for 2D materials: application in noble Metal/TiB

(2) heterointerfaces and their enhanced catalytic performance for formic acid dehydrogenation, Adv. Mater. 33 (2021) e2101536.
[22] H. Chen, J. Fan, Y. Fu, C.-L. Do-Thanh, X. Suo, T. Wang, I. Popovs, D.-e Jiang, Y. Yuan, Z. Yang, S. Dai, Benzene ring knitting achieved by ambient-temperature dehalogenation via mechanochemical Ullmann-type reductive coupling, Adv. Mater. 33 (2021) 2008685.
[23] P. Du, K. Huang, X. Fan, J. Ma, N. Hussain, R. Wang, B. Deng, B. Ge, H. Tang, R. Zhang, M. Lei, H. Wu, Wet-milling synthesis of immobilized Pt/Ir nanoclusters as promising heterogeneous catalysts, Nano Res. 15 (2021) 3065–3072.
[24] H. Wang, X. Wang, J. Pan, L. Zhang, M. Zhao, J. Xu, B. Liu, W. Shi, S. Song, H. Zhang, Ball-milling induced debonding of surface atoms from metal bulk for construing high-performance dual-site single-atom catalysts, Angew. Chem. Int. Ed. 60 (2021) 23154–23158.
[25] G.F. Han, F. Li, A.I. Rykov, Y.K. Im, S.Y. Yu, J.P. Jeon, S.J. Kim, W. Zhou, R. Ge, Z. Ao, T.J. Shin, J. Wang, H.Y. Jeong, J.B. Baek, Abrading bulk metal into single atoms, Nat. Nanotechnol. 17 (2022) 403–407.
[26] M. Li, T. Zhang, S.-Z. Yang, Y. Sun, J. Zhang, F. Polo-Garzon, K.M. Siniard, X. Yu, Z. Wu, D.M. Driscoll, A.S. Ivanov, H. Chen, Z. Yang, S. Dai, Mechanochemistry-induced strong metal–support interactions construction toward enhanced hydrogenation, ACS Catal. 13 (2023) 6114–6125.
[27] Y. Dong, S. Zhang, X. Du, S. Hong, S. Zhao, Y. Chen, X. Chen, H. Song, Boosting the electrical double-layer capacitance of graphene by self-doped defects through ball-milling, Adv. Funct. Mater. 29 (2019) 1901127.
[28] J. Zhang, J. Ma, T.S. Choksi, D. Zhou, S. Han, Y.-F. Liao, H.B. Yang, D. Liu, Z. Zeng, W. Liu, X. Sun, T. Zhang, B. Liu, Strong metal–support interaction boosts activity, selectivity, and stability in electrosynthesis of H2O2, J. Am. Chem. Soc. 144 (2022) 2255–2263.
[29] X. Wang, X. Li, S. Ding, Y. Chen, Y. Liu, M. Fang, G. Xiao, Y. Zhu, Constructing ample active sites in nitrogen-doped carbon materials for efficient electrocatalytic carbon dioxide reduction, Nano Energy 90 (2021) 106541.
[30] P. Gao, J. Jiang, S. Maeda, K. Kubota, H. Ito, Mechanochemically generated calcium-based heavy grignard reagents and their application to carbon-carbon bond-forming reactions, Angew. Chem. Int. Ed. 61 (2022) e202207118.
[31] Y. Lu, H. Kim, K. Sakaki, S. Hayashi, K. Jimura, K. Asano, Destabilizing the dehydrogenation thermodynamics of magnesium hydride by utilizing the immiscibility of Mn with Mg, Inorg. Chem. 58 (2019) 14600–14607.
[32] P.E. Blöchl, Projector augmented-wave method, Phys. Rev. B 50 (1994) 17953–17979.
[33] G. Kresse, J. Hafner, Ab initio molecular-dynamics simulation of the liquid-metal-amorphous-semiconductor transition in germanium, Phys. Rev. B 49 (1994) 14251–14269.
[34] P.P. John, B. Kieron, E. Matthias, Generalized gradient approximation made simple, Phys. Rev. Lett. 77 (1996) 3865.
[35] G. Kresse, J. Furthmüller, Efficiency of ab-initio total energy calculations for metals and semiconductors using a plane-wave basis set, Comput. Mater. Sci. 6 (1996) 15–50.
[36] G. Kresse, D. Joubert, From ultrasoft pseudopotentials to the projector augmented-wave method, Phys. Rev. B 59 (1999) 1758.
[37] S. Grimme, J. Antony, S. Ehrlich, H. Krieg, A consistent and accurate ab initio parametrization of density functional dispersion correction (DFT-D) for the 94 elements H-Pu, J. Chem. Phys. 132 (2010) 154104.
[38] X. Yang, Q. Li, L. Li, J. Lin, X. Yang, C. Yu, Z. Liu, Y. Fang, Y. Huang, C. Tang, CuCo binary metal nanoparticles supported on boron nitride nanofibers as highly efficient catalysts for hydrogen generation from hydrolysis of ammonia borane, J. Power Sources 431 (2019) 135–143.
[39] C. Wang, D. Astruc, Recent developments of nanocatalyzed liquid-phase hydrogen generation, Chem. Soc. Rev. 50 (2021) 3437–3484.